mater.scichina.com link.springer.com

Published online 13 October 2023 | https://doi.org/10.1007/s40843-023-2582-6
Sci China Mater 2023, 66(11): 4387–4395

Synergistically tuning intermediate adsorption and promoting water dissociation to facilitate electrocatalytic nitrate reduction to ammonia over nanoporous Ru-doped Cu catalyst

Yuhuan Cui[1,2†], Changning Sun[1†], Guopeng Ding[1], Ming Zhao[1], Xin Ge[3], Wei Zhang[3], Yongfu Zhu[1*], Zhili Wang[1*] and Qing Jiang[1*]

ABSTRACT **Electrochemical nitrate reduction reaction (NO_3RR) for ammonia generation has garnered attention as an emerging alternative to the energy intensive Haber–Bosch process for sustainable ammonia synthesis and wastewater treatment. However, current NO_3RR still suffers from low ammonia yield and poor selectivity due to the lack of effective electrocatalysts. Here, the bimodal nanoporous Ru-doped Cu catalyst prepared by the dealloying method is reported as an electrocatalyst for NO_3RR, which exhibits an ultrahigh ammonia yield rate of 29.63 ± 0.74 mg h^{-1} $mg_{cat.}^{-1}$ with 97.3% ± 2.5% Faradaic efficiency at −0.2 V *versus* reverse hydrogen electrode, outperforming most of the reported catalysts under similar conditions. Density functional theory calculations reveal that doping Ru into Cu can optimize the adsorption energies of intermediates and lower the energy barrier of the rate-determining step of NO_3RR. Moreover, Ru atom can promote H_2O adsorption/dissociation to supply reactive hydrogen species for N-containing intermediates hydrogenating to ammonia. This work provides a new avenue for the rational design of high-performance catalysts for NO_3RR and other important applications.**

Keywords: nitrate reduction reaction, ammonia synthesis, nanoporous metal, electrocatalysis, density functional theory

INTRODUCTION

Ammonia (NH_3) is one of the most important feedstocks to produce fertilizers, chemicals, pharmaceuticals, and polymers [1–3]. NH_3 is also regarded as a potential carbon-free energy carrier because of its high hydrogen content (17.6 wt%), high energy density (4.32 kW h L^{-1}), and ease of liquefication [4,5]. Currently, the industrial synthesis of NH_3 is heavily dependent on the energy-intensive Haber–Bosch process, which requires high reaction temperature (400–500°C) and pressure (150–300 atm, 1 atm = 1.01 × 10^5 Pa), and complex and large-scale infrastructure [6–8]. Today, the Haber–Bosch process consumes 1%–2% of the world's energy output and generates about 1.4% of global carbon dioxide (CO_2) emissions [9,10]. Therefore, electrochemical routes to NH_3 production under ambient conditions using renewable electricity are highly desirable [11–13]. Recently, the electrochemical nitrate reduction reaction (NO_3RR) is recognized as a promising and sustainable route to the production of NH_3. Compared with the N≡N triple bond in nitrogen (N_2, 941 kJ mol^{-1}), the N=O bond in NO_3^- has a lower dissociation energy (204 kJ mol^{-1}), leading to the faster reaction rate for NH_3 production through NO_3RR compared with N_2 reduction reaction [14–16]. Furthermore, NO_3^- is one of the most widespread water pollutants that can disturb the global nitrogen cycle balance and pose serious health risks to aquatic plants and humans [17,18]. Thus, NO_3RR also provides an avenue to solve the problem of nitrate pollution of ground and drinking water. Currently, electrochemical NO_3RR to NH_3 suffers from slow reaction rate and low NH_3 selectivity because NO_3RR involves eight-electron transfer along with several side reactions [19–21]. Besides, the occurrence of competing hydrogen (H_2) evolution reaction (HER) under electrochemical conditions also reduces the Faradaic efficiency (FE) of NO_3RR to NH_3 [22–24]. Therefore, the development of NO_3RR electrocatalysts with high activity and excellent selectivity is highly desirable but remains a grand challenge.

Copper (Cu) is considered to be one of the most efficient catalysts for NO_3RR and has been investigated intensively [25–27]. In recent years, great efforts have been made to improve the NO_3RR performance of Cu-based catalysts by various strategies such as morphology and structure tuning [28,29], interface engineering [30,31], and alloying [32,33], and the enhanced NH_3 yield rate and Faradaic efficiency (FE_{NH_3}) were achieved. However, to meet the application requirements of NO_3RR for NH_3 production, more efficient catalysts still remain to be developed. Previous computational and experimental studies have shown that the NO_3RR performance of Cu-based catalysts can be improved by tuning the adsorption strengths of reactants and intermediates (such as $*NO_3^-$ and $*NO_2$) on their surfaces [34,35]. For example, Sargent and co-workers [33] achieved a 6-fold increase in NO_3RR activity over $Cu_{50}Ni_{50}$ alloy catalyst

[1] Key Laboratory of Automobile Materials, Ministry of Education, and School of Materials Science and Engineering, Jilin University, Changchun 130022, China
[2] College of Chemistry and Environmental Science, Hebei University, Baoding 071002, China
[3] Key Laboratory of Mobile Materials MOE, and School of Materials Science & Engineering, and Electron Microscopy Center, Jilin University, Changchun 130012, China
† These authors contributed equally to this work.
* Corresponding authors (emails: yfzhu@jlu.edu.cn (Zhu Y); zhiliwang@jlu.edu.cn (Wang Z); jiangq@jlu.edu.cn (Jiang Q))

compared with the case of pure Cu catalyst due to the alloying of Ni with Cu enhancing the adsorption energies of intermediate species on its surface. On the other hand, the NO_3RR to NH_3 involves N-containing intermediate hydrogenation steps, during which active hydrogen (*H) was generated from water (H_2O) splitting and reacted with N-containing intermediates to form NH_3 [36]. Thus, promoting H_2O dissociation to generate *H while inhibiting the dimerization of *H to form H_2 is crucial for enhancing the NO_3RR performance. For example, Yu and co-workers [37] prepared strained ruthenium (Ru) nanoclusters as electrocatalysts for NO_3RR, and demonstrated that the tensile strains facilitate the *H formation but suppress the *H dimerization during H_2O splitting, leading to enhanced NO_3RR performance. However, Cu exhibits poor ability to dissociate H_2O and absorb *H on its surface, which also limits the NO_3RR performance. Therefore, synergistic tuning the electronic structures of Cu-based catalysts to optimize adsorption energies of intermediates of NO_3RR and enhance H_2O adsorption/dissociation would significantly boost the NO_3RR performance, but still remains a great challenge.

Heteroatom doping has been demonstrated as an effective strategy to tune the electronic structure of catalysts to optimize the adsorption strength of intermediates for performance improvement [38,39]. Ru has a higher electronegativity than Cu and possesses excellent performance for H_2O dissociation [40]. The doping of Ru into Cu would improve NO_3RR to NH_3 *via* modulating reactant/intermediate adsorption and enhancing H_2O adsorption/dissociation. In addition, three-dimensional (3D) nanoporous metals prepared by the dealloying method have demonstrated high activity and excellent stability in several catalytic reactions because of the unique bicontinuous nanopore structure, large specific surface area, and high electric conductivity [41–43], and thus are expected to have great potential to improve the NO_3RR performance for NH_3 production. In this work, we employed a facile and scalable alloying/dealloying method to prepare 3D bimodal nanoporous Ru-doped Cu (noted as np Ru-Cu) as an efficient catalyst for NO_3RR to NH_3. The optimized np Ru-Cu catalyst exhibits a high NH_3 yield rate of 29.63 ± 0.74 mg h^{-1} $mg_{cat.}^{-1}$ with corresponding FE_{NH_3} of $97.3\% \pm 2.5\%$ at -0.2 V *versus* reverse hydrogen electrode (RHE), outperforming most of the reported catalysts under similar conditions. Density functional theory (DFT) calculations demonstrate that the doping of Ru with Cu can modulate the adsorption energies of intermediates, reduce the energy barrier of the rate-determining step (RDS) of NO_3RR, and enhance H_2O adsorption/dissociation to supply *H for N-containing intermediate hydrogenation to form NH_3, leading to an extraordinary NO_3RR performance.

EXPERIMENTAL SECTION

Synthesis of np Ru-Cu catalyst

The np Ru-Cu catalyst was fabricated by a facile and scalable alloying/dealloying procedure. First, the oxides on the surface of pure Al, Cu and Ru metals were initially removed in 0.5 mol L^{-1} H_2SO_4 solution. For the synthesis of np Ru-Cu catalyst with the Ru content of 3.0 at%, the $Al_{88}Cu_{11.4}Ru_{0.6}$ alloy precursors were prepared by an arc melting method using pure Al, Cu and Ru metals with a specific ratio. The obtained alloy ingot was then re-melted in a quartz tube and subsequently injected onto a rotating Cu wheel under Ar atmosphere to make $Al_{88}Cu_{11.4}Ru_{0.6}$ alloy ribbons. Finally, the alloy ribbons were immersed into 1.0 mol L^{-1} KOH solution at room temperature for 5 h. After 5 h, the production was filtered and rinsed with H_2O and ethanol for several times to remove the impurity ions in the solution. For comparison, np Cu and various np Ru-Cu catalysts with the Ru contents of 1.8, 5.0, and 7.8 at% were also prepared by the same preparation method using $Al_{88}Cu_{12}$, $Al_{88}Cu_{11.7}Ru_{0.3}$, $Al_{88}Cu_{10.8}Ru_{1.2}$ and $Al_{88}Cu_{9.6}Ru_{2.4}$ alloy ribbons as precursors, respectively.

Synthesis of Ru-Cu NPs

The Ru-doped Cu nanoparticles (Ru-Cu NPs) were fabricated by a wet chemical reduction method. First, 1 mL $CuCl_2{\cdot}2H_2O$ (0.1 mol L^{-1}) and 30 μL $RuCl_3{\cdot}xH_2O$ (0.1 mol L^{-1}) solutions were added into 30 mL H_2O containing 0.05 g polyvinyl pyrrolidone (PVP). Then $NaBH_4$ solution (0.2 mol L^{-1}, 10 mL) was poured into the above mixture under stirring at room temperature for 30 min, after which the sample was separated by centrifugation, washed with H_2O for three times, and then dried in vacuum at room temperature overnight.

Electrochemical measurements

Catalytic ink was prepared by dispersing 5.0 mg catalysts in 1.0 mL mixed solution containing 720 μL ethanol, 240 μL H_2O and 40 μL Nafion (5 wt%) and ultrasonicated for 1 h. Then, 10 μL catalytic ink was loaded on a piece of carbon paper (1 cm^2) with the catalyst mass loading of 0.05 mg cm^{-2} and dried at room temperature. The electrochemical measurements were conducted under Ivium electrochemical workstation in a H-type electrolytic cell separated by a piece of Nafion 115 membrane. The Nafion 115 membrane was pretreated by 5% H_2O_2 solution (1 h), deionized (DI) water (1 h), 0.5 mol L^{-1} H_2SO_4 solution (1 h) and DI water (1 h) in turn under 80°C water bath. Ag/AgCl and platinum foil were used as the reference electrode and counter electrode, respectively. The applied potentials were converted to the RHE, E (*versus* RHE) = E (*versus* Ag/AgCl) + $0.197 + 0.059 \times$ pH. The onset potential was identified where the current density reaches -2 mA cm^{-2}. Before the electrochemical measurements, Ar gas was purged into the electrolyte solution for at least 30 min to avoid the influence of air. The NO_3RR measurements were tested three times for accuracy.

Microstructural and chemical characterizations

X-ray diffraction (XRD) was conducted using Cu-Kα radiation on a D/max2500pc diffractometer. The scanning electron microscopy (SEM) and SEM-energy dispersive X-ray spectroscopy (EDS) were characterized using an SEM (JEOL JSM-7900F, 15 keV). The electron micrographic structures were characterized by transmission electron microscopy (TEM, JEOL, JEM-2100F, 200 kV) and spherical aberration-corrected TEM (JEM-ARM300F). X-ray photoelectron spectroscopy (XPS) analysis was analyzed using an ESCALAB 250Xi system. The H_2 and N_2 gases were detected through the gas chromatograph (Shimadzu GC-2014) equipped with a thermal conductivity detector. The compositions of catalysts were analyzed by inductively coupled plasma optical emission spectroscopy (ICP-OES, Thermo electron). Ultraviolet-visible (UV-Vis) absorption spectra were recorded on an UV-2600i spectrophotometer. For the isotopic labeling experiments, the $^{15}NH_4^+$ and $^{14}NH_4^+$ were detected by ^{1}H nuclear magnetic resonance (^{1}H NMR, Bruker,

AVANCE III HD, 500 M).

RESULTS AND DISCUSSION

Synthesis and characterizations of np Ru-Cu catalysts

The 3D bimodal np Ru-Cu catalyst was prepared by a facile and scalable alloying/dealloying method, as illustrated in Fig. S1. In a typical synthesis, the $Al_{88}Cu_{11.4}Ru_{0.6}$ alloy ribbons were first prepared by arc-melting/melting-spinning processes from pure Al, Cu, and Ru metals with the certain atomic ratio (Fig. S2a). XRD pattern shows that the as-prepared $Al_{88}Cu_{11.4}Ru_{0.6}$ alloy ribbons are composed of α-Al, intermetallic $CuAl_2$ and Al_6Ru phases (Fig. S2b) [42]. The np Ru-Cu catalyst was then fabricated by immersing the $Al_{88}Cu_{11.4}Ru_{0.6}$ alloy ribbons in 1.0 mol L^{-1} KOH aqueous solution for 5 h at room temperature, by which method Al element was dissolved from α-Al phase to form large pores as well as from $CuAl_2$ and Al_6Ru phase to form small nanopores. SEM image of np Ru-Cu shows that the product exhibits a hierarchical porous structure consisting of macropores with an average pore size of ~212 nm and mesopores with an average pore size of ~26 nm (Fig. 1a and Fig. S3). It is worthy to point out that such a bimodal porous structure not only facilitates the penetration of electrolytes through large pores, but offers abundant active sites for NO_3RR by virtue of the small nanopores [44]. The atomic-resolution high-angle annual dark-field scanning TEM (HAADF-STEM) and the corresponding fast Fourier transform (FFT) pattern clearly reveal that the np Ru-Cu catalyst exhibits high crystallinity with a face-centered cubic (fcc) structure (Fig. 1b) [41]. The interplanar spacing was measured to be 0.211 nm, which is slightly larger than that of the Cu(111) face (0.209 nm), demonstrating the doping of larger Ru atoms into the Cu lattice. STEM image and the corresponding EDS elemental mapping show the homogenous distribution of Ru and Cu throughout the ligament (Fig. 1c). Further element line scanning indicates that Ru atoms are separately embedded in Cu atomic arrays (Fig. S4). The content of Ru in the np Ru-Cu catalyst was determined by ICP-OES to be 3.0 at%, which is consistent with the result obtained using TEM and EDS (Fig. S5). XRD pattern shows that the np Ru-Cu catalyst has a face-centered cubic structure, where the peaks observed at 43.3°, 50.4°, 74.1°, and 89.9° can be assigned to the (111), (200), (220), and (311) planes of the fcc Cu crystal (Fig. 1d) [45]. No diffraction peaks of Ru were observed in the XRD pattern, demonstrating that no pure Ru phase exists in np Ru-Cu. Additionally, the diffraction peaks of np Ru-Cu catalyst negatively shifted to lower angles compared with those of np Cu catalyst, further indicating that Ru is incorporated into the Cu structure, which is consistent with the HAADF-STEM observations. XPS further confirms the presence of Ru and Cu in np Ru-Cu catalyst. The high-resolution Ru 3p XPS spectrum shows two peaks with the binding energies of 462.5 and 484.4 eV, which correspond to Ru $3p_{3/2}$ and Ru $3p_{1/2}$ for metallic Ru^0 species, respectively (Fig. 1e) [46]. The high-resolution Cu 2p XPS spectrum shows two main peaks at 932.8 and 952.6 eV, which are assigned to Cu $2p_{3/2}$ and Cu $2p_{1/2}$ of metallic Cu^0, respectively, indicating that Cu in np Ru-Cu catalyst is mainly in the metallic state (Fig. 1f) [47]. It is worth noting that the binding energy of Cu $2p_{3/2}$ for np Ru-Cu shows a distinct shift of 0.12 eV towards higher binding energy compared with np Cu, suggesting that the doping of Ru results in the transfer of elec-

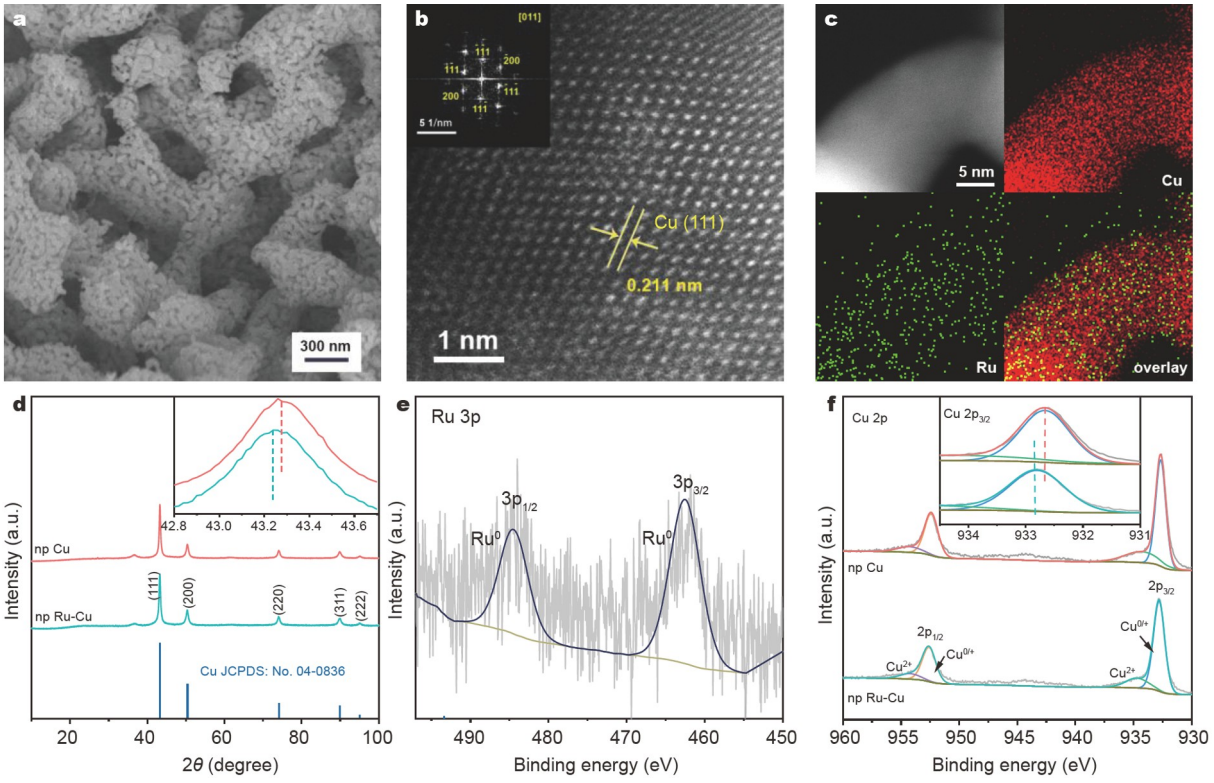

Figure 1 Structural characterization of the np Ru-Cu catalyst. (a) SEM and (b) HAADF-HRTEM images of np Ru-Cu catalyst (the inset is the FFT pattern of np Ru-Cu catalyst). (c) TEM image and corresponding EDS elemental maps of np Ru-Cu catalyst. (d) XRD patterns of np Ru-Cu and np Cu catalysts. (e) Ru 3p XPS spectrum of np Ru-Cu catalyst and (f) Cu 2p XPS spectra of np Ru-Cu and np Cu catalysts.

trons from Cu to Ru in np Ru-Cu catalyst. As a control, np Cu without Ru doping was also prepared through the same method as np Ru-Cu catalyst except using $Al_{88}Cu_{12}$ alloy ribbons as precursors. EDS, XRD, SEM and TEM characterizations (Fig. S6) show that the np Cu catalyst has similar morphology and crystal structure as np Ru-Cu catalyst.

Electrochemical NO_3RR performance

The electrochemical NO_3RR performance of np Ru-Cu and np Cu catalysts were investigated under ambient conditions in a standard three-electrode H-type cell. The linear sweep voltammetry (LSV) curves show that the np Ru-Cu catalyst delivers much larger current density than that of the np Cu catalyst under the same potential in the presence of NO_3^- ions (Fig. 2a). Moreover, the np Ru-Cu catalyst exhibits an onset potential of 0.23 V *versus* RHE, which is more positive than that of np Cu (0.12 V *versus* RHE). The larger current density and higher onset potential demonstrate that the np Ru-Cu catalyst is much more active in electrocatalyzing reduction of NO_3^- than the np Cu catalyst. To further assess the NH_3 yield rate and FE_{NH_3} of np Ru-Cu catalyst, the constant-potential electrolysis experiments were carried out in Ar-saturated 0.1 mol L^{-1} KOH aqueous solution with 50 mmol L^{-1} KNO_3 under a series of potentials from 0.1 to −0.3 V *versus* RHE for 2 h. The produced NH_3 was quantified based on the UV-Vis absorbance spectra with the calibration curves established by the indophenol blue method (Fig. S7). As shown in Fig. 2b, for the np Ru-Cu catalyst, the NH_3 yield rate gradually increases as the potential negatively shifts. However, the FE_{NH_3} increases with the negative potential increasing until −0.2 V *versus* RHE and then decreases (Fig. 2c). Combining the NH_3 yield rate and FE_{NH_3}, the optimal potential for np Ru-Cu catalyst towards electrochemical NO_3^--NH_3 conversion is −0.2 V *versus* RHE. At this potential, the np Ru-Cu catalyst exhibits the highest FE_{NH_3} of 97.3% ± 2.5% with an NH_3 yield rate of 29.63 ± 0.74 mg h^{-1} $mg_{cat.}^{-1}$, which are almost 2.0 and 3.5 times higher than that of the np Cu catalyst (47.7% ± 0.4% and 8.20 ± 0.16 mg h^{-1} $mg_{cat.}^{-1}$, respectively). It should be noted that the np Ru-Cu catalyst also exhibits the FE_{NH_3} of 77.4% ± 3.9% at the positive potential of 0.1 V *versus* RHE, whereas the np Cu catalyst gives the FE_{NH_3} of only 3.9% ± 0.78%. To compare the intrinsic activities of np Ru-Cu and np Cu catalysts, the specific activities were normalized by the electrochemically active surface areas (ECSAs) that were determined by means of electrochemical double-layer capacitance (C_{dl}) (Fig. S8a–c) [31,48]. As shown in Fig. S8d, the np Ru-Cu

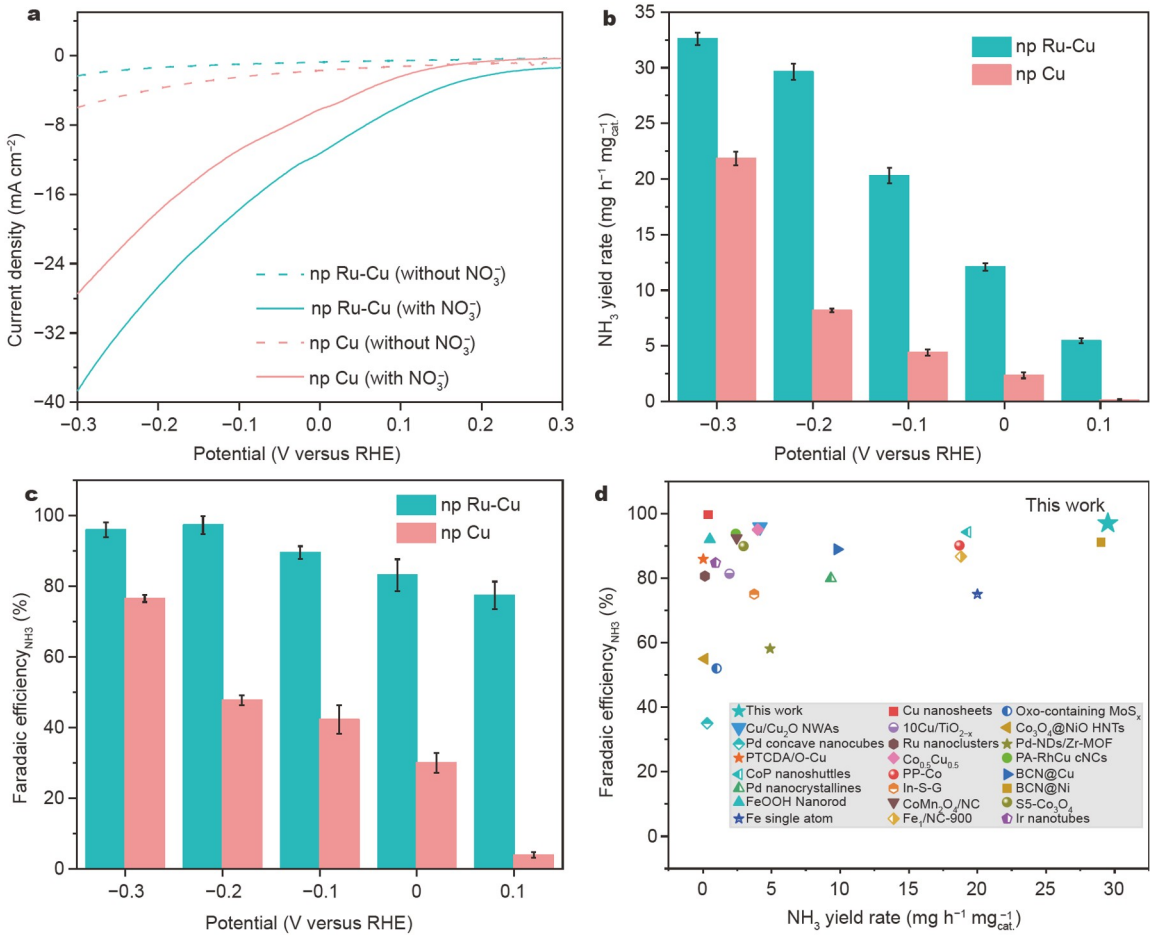

Figure 2 Electrochemical NO_3RR performances. (a) LSV curves of np Ru-Cu and np Cu catalysts in Ar-saturated 0.1 mol L^{-1} KOH with and without 50 mmol L^{-1} NO_3^- (scan rate: 20 mV s^{-1}). Comparisons of (b) NH_3 yield rate and (c) FE_{NH_3} between np Ru-Cu and np Cu catalysts. (d) Comparison of NH_3 yield rate and FE_{NH_3} of the np Ru-Cu catalyst with other recently reported catalysts.

catalyst exhibits a specific activity of 1.77 mg h^{-1} cm_{ECSA}^{-2} at −0.2 V *versus* RHE, higher than that of the np Cu catalyst (0.38 mg h^{-1} cm_{ECSA}^{-2}). These results demonstrate that the enhanced electrocatalytic performance of np Ru-Cu originates from its higher intrinsic activity. Based on the above result, it can be considered that the doping of Ru into Cu significantly improves the catalytic activity and NH_3 selectivity of NO_3RR for NH_3 production. To investigate the importance of nanoporous structure, Ru-Cu NPs with the average size of ~18 nm were synthesized for NO_3RR through a wet-chemical reduction method (Fig. S9a–c). It was found that the NH_3 yield rate and FE_{NH_3} of Ru-Cu NPs are lower than those of np Ru-Cu at all the tested potentials (Fig. S9f), suggesting hierarchical nanoporous structure is beneficial for NO_3RR. It is worth noting that the NO_3RR performance including NH_3 yield rate and FE_{NH_3} of our np Ru-Cu catalyst have exceeded most of recently reported electrocatalysts under similar conditions (Fig. 2d, see Table S1 for more details).

The possible by-products such as NO_2^-, N_2H_4, N_2 and H_2 over the np Ru-Cu catalyst were also detected. The generation of NO_2^- was measured by UV-Vis spectrophotometry. The FE of NO_2^- at 0.1 V *versus* RHE is about 20% and then gradually decreases to 1.9% at −0.2 V *versus* RHE (Fig. S10). This decline trend inversely correlates to the gradual increase of NH_3 selectivity, suggesting that NO_2^- is the intermediate product and can be further reduced to NH_3 under more negative potentials [10]. In addition, no N_2H_4 was detected by the UV-Vis spectrophotometry in our system (Fig. S11). The gas by-products of H_2 and N_2 gases were measured by gas chromatography, and the result shows that no detectable signals for H_2 and N_2 at −0.2 V *versus* RHE (Fig. S12), suggesting that np Ru-Cu catalysts could effectively suppress H_2 and N_2 production. These results suggest that the np Ru-Cu catalyst also has an excellent NH_3 selectivity towards the electrochemical NO_3^--NH_3 conversion.

Since Ru in np Ru-Cu catalyst plays a key role in improving NO_3RR activity and NH_3 selectivity, the influence of Ru content on the NO_3RR performance was also investigated. For this end, various np Ru-Cu catalysts with Ru contents of 1.8, 5.0, and 7.8 at% (measured by ICP-OES) were prepared by the same preparation method using $Al_{88}Cu_{11.7}Ru_{0.3}$, $Al_{88}Cu_{10.8}Ru_{1.2}$ and $Al_{88}Cu_{9.6}Ru_{2.4}$ alloy ribbons as precursors, respectively. SEM characterizations show that these samples have similar bimodal nanoporous structures (Fig. S13). XRD results show that no Ru phase appears in these samples when increasing Ru contents to 5.0 and 7.8 at% (Fig. S14). Electrochemical studies show that both the NH_3 yield rate and FE_{NH_3} increase with increasing the Ru content up to 3.0 at% and then decrease when further increase the Ru content (Fig. S15). The above results demonstrate that the NO_3RR performance is strongly affected by the Ru content and the optimal Ru content is 3.0 at% for np Ru-Cu catalysts. Above the optimal content, excessive Ru atoms may cover some Cu atoms, resulting in the decrease of available active sites and leading to reduced NO_3RR performance.

The isotopic labeling experiments using $^{15}NO_3^-$ and $^{14}NO_3^-$ as reagents coupled with ^1H NMR analysis were conducted to verify the N source of the detected NH_3 during NO_3RR [8]. As shown in Fig. 3a, only two peaks corresponding to $^{15}NH_4^+$ were observed in the ^1H NMR spectrum when using $^{15}NO_3^-$ as the reagent. Moreover, three peaks corresponding to $^{14}NH_4^+$ were detected in the ^1H NMR spectrum when using $^{14}NO_3^-$ as the reagent, and no NH_4^+ signals can be detected without NO_3^- in the electrolyte. These results indicate that the obtained NH_3 is produced *via* electrochemical NO_3^--NH_3 conversion rather than any other contaminations in the system. The produced NH_3 was further quantitatively determined by the ^1H NMR spectroscopy (Fig. S16). The NH_3 yield rate and FE_{NH_3} of np Ru-Cu were calculated by ^1H NMR method to be 28.99 mg h^{-1} $mg_{cat.}^{-1}$ and 95.3%, respectively, which are very close to the results from the UV-Vis method (Fig. 3b), suggesting the accuracy of quantitative methods.

Since different nitrate sources usually contain a wide range of NO_3^- concentrations, the catalytic performance of np Ru-Cu catalyst under different NO_3^- concentrations were also investigated. Increased current densities were observed with the increase of NO_3^- concentrations (Fig. S17). As shown in Fig. 3c, the NH_3 yield rate increases from 0.94 ± 0.04 to 34.60 ± 0.43 mg h^{-1} $mg_{cat.}^{-1}$ when the NO_3^- concentration increases from 1 to 100 mmol L^{-1}. The FE_{NH_3} increases from 19.3% ± 0.8% (1 mmol L^{-1} NO_3^-) to 97.3% ± 2.5% (50 mmol L^{-1} NO_3^-), and then slightly decreases to 82.0% ± 2.5% (100 mmol L^{-1} NO_3^-). The slightly reduced FE_{NH_3} under higher NO_3^- concentration may result from the deactivation of the active sites because the produced NH_3 can not be removed rapidly from the catalyst surface in time. Considering that the sewage and industrial wastewater usually contain some NO_2^- ions, the electrocatalytic NO_2^- reduction performance of np Ru-Cu catalyst was also investigated in 0.1 mol L^{-1} KOH solution containing 50 mmol L^{-1} NO_2^-. The NH_3 yield rate of 41.9 mg h^{-1} $mg_{cat.}^{-1}$ and FE_{NH_3} of 96.5% are obtained at −0.3 V *versus* RHE (Fig. S18). These results demonstrate promising application potential of the np Ru-Cu catalyst for sewage and industrial wastewater treatment.

The electrochemical durability of the np Ru-Cu catalyst for NO_3RR was also evaluated. As shown in Fig. 3d, there are no obvious attenuation in both the NH_3 yield rate and FE_{NH_3} during 15 cycles. In addition, SEM, XRD, and XPS characterizations reveal that the bimodal nanoporous morphology, the crystalline structure, and chemical valence states maintained well after the durability test (Fig. S19). These results confirm that the np Ru-Cu catalyst has an excellent stability under present experimental conditions.

DFT calculations

To gain further insight into the origin of the enhanced activity of Ru-Cu catalyst for NO_3RR, DFT calculations were performed. The Cu(111) and Ru-Cu(111) facets were constructed for DFT calculations because they have the lowest formation energies among the different facets (Fig. S20). The Hirshfeld charge analysis shows that some electrons transfer from Cu atoms to Ru atom (Fig. S21), which is agree with the XPS results. The project density of state (PDOS) analysis shows that the d-band center of Ru-Cu (−2.41 eV) moves towards the Fermi energy compared with Cu (−2.68 eV) (Fig. 4a). It is well known that for transition metals, the higher the d-band center, the stronger interaction between the catalysts and reaction intermediates [49]. For Ru-Cu, the up-shift of d-band center leads to stronger adsorption of intermediates on its surface. Since the adsorption of NO_3^- is the first step during NO_3RR and plays an important role in the

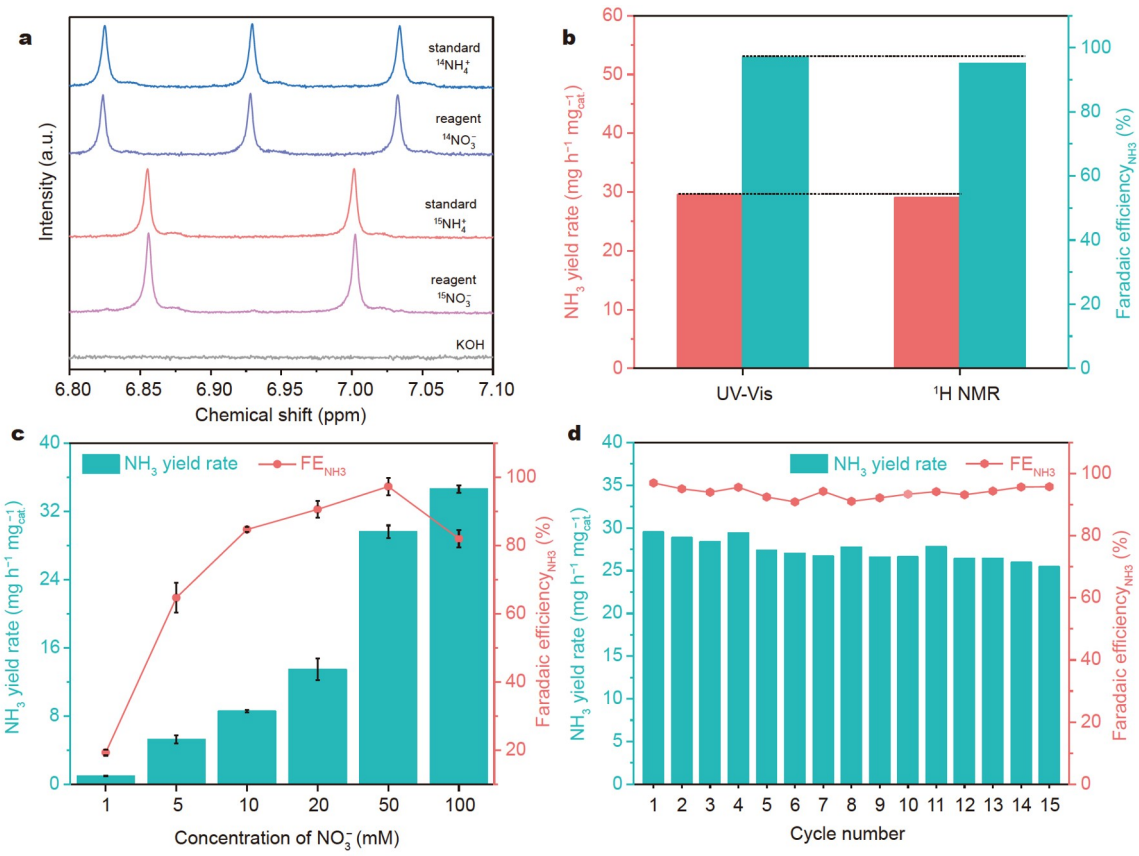

Figure 3 Electrochemical NO_3RR performances. (a) ^{1}H NMR spectra from NO_3RR at −0.2 V *versus* RHE using $^{14}NO_3^-$ or $^{15}NO_3^-$ as the reagent and comparison with the standard $^{14}NH_4^+$ and $^{15}NH_4^+$. (b) Comparison of NH_3 yield rate and FE_{NH_3} of np Ru-Cu catalyst determined by the ^{1}H NMR method and indophenol blue method. (c) NH_3 yield rate and FE_{NH_3} of np Ru-Cu catalyst under different NO_3^- concentrations. (d) Recycling test of np Ru-Cu catalyst at −0.2 V *versus* RHE under ambient conditions.

whole catalytic reaction [33,35], the adsorption energies of NO_3^- ($E_{ad\text{-}NO_3^-}$) on the Ru-Cu and Cu were investigated. As shown in Fig. 4b, for Ru-Cu, NO_3^- is adsorbed on the bridge site of Ru and Cu atoms with a vertical configuration, and the $E_{ad\text{-}NO_3^-}$ is calculated to be −2.91 eV, which is stronger than that on the Cu (−2.69 eV). Previous studies have demonstrated that properly enhancing the NO_3^- adsorption strength can improve the NO_3RR performance of Cu-based catalysts [50–52]. Therefore, the enhanced adsorption energy of NO_3^- on Ru-Cu may lead to an improvement of NO_3RR activity. Additionally, the slices of the charge density difference indicate that the electron redistribution caused by Ru doping results in asymmetry electron structure of $*NO_3$, which is in favor of activating the covalent bond of NO_3^-. Fig. 4d, f depict the Gibbs free energy (ΔG) diagrams of the entire NO_3RR process on Ru-Cu and Cu at $U = 0$ V *versus* RHE and the corresponding geometric structures of intermediates, respectively. The NO_3RR process on both Ru-Cu and Cu includes gradual deoxygenation steps to form *N and subsequent hydrogenation steps to produce NH_3, which is in agreement with previous reports of Cu-based catalysts for NO_3RR [27,53]. The conversion of $*NO_2$ to form *NOOH is the RDS for Cu with the ΔG of 0.56 eV, while the RDS for Ru-Cu is the step of $*NO_3 \rightarrow *NO_2OH$ with a smaller ΔG of 0.36 eV, indicating that NO_3^- is more readily reduced on Ru-Cu than Cu, resulting in the enhanced NO_3RR performance.

In alkaline aqueous environment, H_2O molecules serve as the hydrogen source for NO_3RR to NH_3. The dissociation of H_2O to generate *H and suppression of H_2 formation of from *H are both significant for promoting NO_3RR performance. Thus, the absorption energy of H_2O ($E_{ad\text{-}H_2O}$) and the dissociation energy of H_2O on Cu and Ru-Cu were also examined. It was found that the adsorption site of H_2O molecules on Ru-Cu and Cu are the top sites of Ru and Cu atoms, respectively (Fig. 4e). Ru-Cu displays higher $E_{ad\text{-}H_2O}$ (−0.62 eV) than Cu (−0.35 eV), implying stronger H_2O adsorption, which accelerates H_2O dissociation [54]. Moreover, Ru-Cu exhibits a much lower energy barrier of H_2O dissociation (0.01 eV) than Cu (0.15 eV) (Fig. 4e), suggesting the dissociation of H_2O to generate *H on the surface of Ru-Cu is much easier than that of Cu surface. In addition, Ru-Cu has an enhanced *H adsorption energy (−0.53 eV) compared with Cu (−0.33 eV), which is beneficial to gather *H for N-containing intermediate hydrogenation to form NH_3 (Fig. 4c). However, the ΔG value of H_2 formation (0.33 eV) on the Ru-Cu is more positive than that of Cu (0.02 eV), suggesting the dimerization of *H to form H_2 is suppressed and thus the selective electroreduction of NO_3^- into NH_3 can be achieved on Ru-Cu. Thus, Ru-Cu can provide sufficient *H *via* H_2O splitting to hydrogenate the N-containing intermediates for NH_3 generation, enhancing the NO_3RR performance. From the experimental and DFT calculations results, it can be concluded that

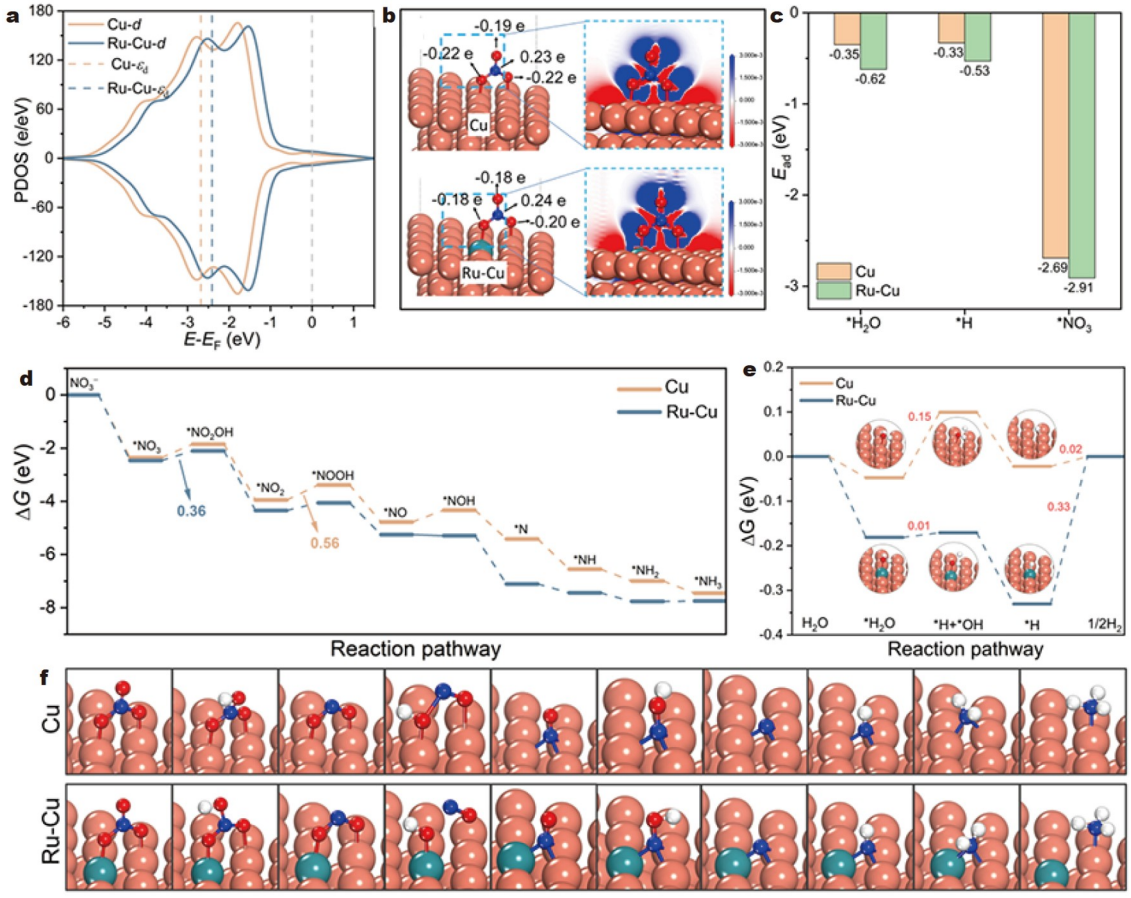

Figure 4 DFT calculations. (a) PDOS with d-band center of Ru-Cu and Cu. (b) Configurations and charge density difference slices of NO_3^- adsorption on Ru-Cu and Cu surfaces. (c) *H_2O, *H and *NO_3 adsorption energies on Ru-Cu and Cu surfaces. Gibbs free energy changes of (d) NO_3RR and (e) HER on Ru-Cu and Cu surfaces. (f) Geometric structures of intermediates during NO_3RR on Cu and Ru-Cu surfaces. Color code: orange, Cu; green, Ru; red, O; blue, N; white, H; the asterisk * denotes an adsorption state.

synergistically optimizing the intermediate adsorption energy and promoting H_2O adsorption/dissociation through Ru doping is a significant contributor to the enhanced NO_3RR performance of np Ru-Cu catalyst.

CONCLUSIONS

In summary, we have synthesized a highly active and selective np Ru-Cu catalyst for the electrochemical reduction of NO_3^- to NH_3. The optimal np Ru-Cu catalyst exhibits a high NH_3 yield rate of 29.63 ± 0.74 mg h^{-1} $mg_{cat.}^{-1}$ with the corresponding FE_{NH_3} of 97.3% ± 2.5% at −0.2 V *versus* RHE, which are much higher than those obtained for most of the reported catalysts under similar conditions. Furthermore, the np Ru-Cu catalyst also shows excellent stability under the present experimental conditions. DFT calculations reveal that the outstanding NO_3RR performance of np Ru-Cu catalyst is associated with the optimized adsorption energies of intermediates, the reduced free energy of RDS, and the promoted adsorption/dissociation of H_2O through Ru doping. This work not only provides an efficient and stable catalyst in electrochemical NO_3RR for NH_3 production, but also paves a way for the rational design of high-performance catalysts for electrochemical NO_3RR and other important chemical and electrochemical reactions.

Received 14 June 2023; accepted 17 August 2023; published online 13 October 2023

1 Rosca V, Duca M, de Groot MT, *et al.* Nitrogen cycle electrocatalysis. Chem Rev, 2009, 109: 2209–2244
2 Chen JG, Crooks RM, Seefeldt LC, *et al.* Beyond fossil fuel-driven nitrogen transformations. Science, 2018, 360: eaar6611
3 Canfield DE, Glazer AN, Falkowski PG. The evolution and future of Earth's nitrogen cycle. Science, 2010, 330: 192–196
4 Zhu X, Mou S, Peng Q, *et al.* Aqueous electrocatalytic N_2 reduction for ambient NH_3 synthesis: Recent advances in catalyst development and performance improvement. J Mater Chem A, 2020, 8: 1545–1556
5 Shen H, Choi C, Masa J, *et al.* Electrochemical ammonia synthesis: Mechanistic understanding and catalyst design. Chem, 2021, 7: 1708–1754
6 Andersen SZ, Čolić V, Yang S, *et al.* A rigorous electrochemical ammonia synthesis protocol with quantitative isotope measurements. Nature, 2019, 570: 504–508
7 Chu K, Liu Y, Cheng Y, *et al.* Synergistic boron-dopants and boron-induced oxygen vacancies in MnO_2 nanosheets to promote electrocatalytic nitrogen reduction. J Mater Chem A, 2020, 8: 5200–5208
8 Cui Y, Dong A, Qu Y, *et al.* Theory-guided design of nanoporous CuMn alloy for efficient electrocatalytic nitrogen reduction to ammonia. Chem Eng J, 2021, 426: 131843
9 Choi C, Gu GH, Noh J, *et al.* Understanding potential-dependent competition between electrocatalytic dinitrogen and proton reduction reactions. Nat Commun, 2021, 12: 4353

10 He W, Zhang J, Dieckhöfer S, *et al.* Splicing the active phases of copper/cobalt-based catalysts achieves high-rate tandem electroreduction of nitrate to ammonia. Nat Commun, 2022, 13: 1129
11 Wang P, Chang F, Gao W, *et al.* Breaking scaling relations to achieve low-temperature ammonia synthesis through LiH-mediated nitrogen transfer and hydrogenation. Nat Chem, 2017, 9: 64–70
12 Cui X, Tang C, Zhang Q. A review of electrocatalytic reduction of dinitrogen to ammonia under ambient conditions. Adv Energy Mater, 2018, 8: 1800369
13 Suryanto BHR, Wang D, Azofra LM, *et al.* MoS_2 polymorphic engineering enhances selectivity in the electrochemical reduction of nitrogen to ammonia. ACS Energy Lett, 2019, 4: 430–435
14 Martínez J, Ortiz A, Ortiz I. State-of-the-art and perspectives of the catalytic and electrocatalytic reduction of aqueous nitrates. Appl Catal B-Environ, 2017, 207: 42–59
15 Duca M, Koper MTM. Powering denitrification: The perspectives of electrocatalytic nitrate reduction. Energy Environ Sci, 2012, 5: 9726–9742
16 Wang Y, Yu Y, Jia R, *et al.* Electrochemical synthesis of nitric acid from air and ammonia through waste utilization. Natl Sci Rev, 2019, 6: 730–738
17 Su L, Han D, Zhu G, *et al.* Tailoring the assembly of iron nanoparticles in carbon microspheres toward high-performance electrocatalytic denitrification. Nano Lett, 2019, 19: 5423–5430
18 Ascott MJ, Gooddy DC, Wang L, *et al.* Global patterns of nitrate storage in the vadose zone. Nat Commun, 2017, 8: 1416
19 Wang Y, Wang C, Li M, *et al.* Nitrate electroreduction: Mechanism insight, *in situ* characterization, performance evaluation, and challenges. Chem Soc Rev, 2021, 50: 6720–6733
20 Han S, Wang C, Wang Y, *et al.* Electrosynthesis of nitrate *via* the oxidation of nitrogen on tensile-strained palladium porous nanosheets. Angew Chem Int Ed, 2021, 60: 4474–4478
21 Liang J, Liu Q, Alshehri AA, *et al.* Recent advances in nanostructured heterogeneous catalysts for N-cycle electrocatalysis. Nano Res Energy, 2022, 1: e9120010
22 Liang J, Li Z, Zhang L, *et al.* Advances in ammonia electrosynthesis from ambient nitrate/nitrite reduction. Chem, 2023, 9: 1768–1827
23 Song W, Yue L, Fan X, *et al.* Recent progress and strategies on the design of catalysts for electrochemical ammonia synthesis from nitrate reduction. Inorg Chem Front, 2023, 10: 3489–3514
24 Zhang W, Qin X, Wei T, *et al.* Single atomic cerium sites anchored on nitrogen-doped hollow carbon spheres for highly selective electroreduction of nitric oxide to ammonia. J Colloid Interface Sci, 2023, 638: 650–657
25 Liu H, Lang X, Zhu C, *et al.* Efficient electrochemical nitrate reduction to ammonia with copper-supported rhodium cluster and single-atom catalysts. Angew Chem Int Ed, 2022, 61: e202202556
26 Fu X, Zhao X, Hu X, *et al.* Alternative route for electrochemical ammonia synthesis by reduction of nitrate on copper nanosheets. Appl Mater Today, 2020, 19: 100620
27 Chen FY, Wu ZY, Gupta S, *et al.* Efficient conversion of low-concentration nitrate sources into ammonia on a Ru-dispersed Cu nanowire electrocatalyst. Nat Nanotechnol, 2022, 17: 759–767
28 Zhao X, Li X, Zhang H, *et al.* Atomic-dispersed copper simultaneously achieve high-efficiency removal and high-value-added conversion to ammonia of nitrate in sewage. J Hazard Mater, 2022, 424: 127319
29 Lim J, Liu CY, Park J, *et al.* Structure sensitivity of Pd facets for enhanced electrochemical nitrate reduction to ammonia. ACS Catal, 2021, 11: 7568–7577
30 Fu W, Hu Z, Zheng Y, *et al.* Tuning mobility of intermediate and electron transfer to enhance electrochemical reduction of nitrate to ammonia on Cu_2O/Cu interface. Chem Eng J, 2022, 433: 133680
31 Cui Y, Dong A, Zhou Y, *et al.* Interfacially engineered nanoporous Cu/MnO_x hybrids for highly efficient electrochemical ammonia synthesis *via* nitrate reduction. Small, 2023, 19: 2207661
32 Cerrón-Calle GA, Fajardo AS, Sánchez-Sánchez CM, *et al.* Highly reactive Cu-Pt bimetallic 3D-electrocatalyst for selective nitrate reduction to ammonia. Appl Catal B-Environ, 2022, 302: 120844
33 Wang Y, Xu A, Wang Z, *et al.* Enhanced nitrate-to-ammonia activity on copper-nickel alloys *via* tuning of intermediate adsorption. J Am Chem Soc, 2020, 142: 5702–5708
34 Wang Z, Richards D, Singh N. Recent discoveries in the reaction mechanism of heterogeneous electrocatalytic nitrate reduction. Catal Sci Technol, 2021, 11: 705–725
35 Niu H, Zhang Z, Wang X, *et al.* Theoretical insights into the mechanism of selective nitrate-to-ammonia electroreduction on single-atom catalysts. Adv Funct Mater, 2020, 31: 2008533
36 Fan K, Xie W, Li J, *et al.* Active hydrogen boosts electrochemical nitrate reduction to ammonia. Nat Commun, 2022, 13: 7958
37 Li J, Zhan G, Yang J, *et al.* Efficient ammonia electrosynthesis from nitrate on strained ruthenium nanoclusters. J Am Chem Soc, 2020, 142: 7036–7046
38 Ding J, Hou X, Qiu Y, *et al.* Iron-doping strategy promotes electroreduction of nitrate to ammonia on MoS_2 nanosheets. InOrg Chem Commun, 2023, 151: 110621
39 Wei T, Bao H, Wang X, *et al.* Ionic liquid-assisted electrocatalytic NO reduction to NH_3 by P-doped MoS_2. ChemCatChem, 2023, 15: e202201411
40 Bae SY, Mahmood J, Jeon IY, *et al.* Recent advances in ruthenium-based electrocatalysts for the hydrogen evolution reaction. Nanoscale Horiz, 2020, 5: 43–56
41 Wan W, Zhou Y, Zeng S, *et al.* Nanoporous intermetallic Cu_3Sn/Cu hybrid electrodes as efficient electrocatalysts for carbon dioxide reduction. Small, 2021, 17: e2100683
42 Shi H, Zhou YT, Yao RQ, *et al.* Spontaneously separated intermetallic Co_3Mo from nanoporous copper as versatile electrocatalysts for highly efficient water splitting. Nat Commun, 2020, 11: 2940
43 Yao RQ, Zhou YT, Shi H, *et al.* Nanoporous surface high-entropy alloys as highly efficient multisite electrocatalysts for nonacidic hydrogen evolution reaction. Adv Funct Mater, 2021, 31: 2009613
44 Tan Y, Liu P, Chen L, *et al.* Monolayer MoS_2 films supported by 3D nanoporous metals for high-efficiency electrocatalytic hydrogen production. Adv Mater, 2014, 26: 8023–8028
45 Liu X, Wang A, Li L, *et al.* Structural changes of Au-Cu bimetallic catalysts in CO oxidation: *In situ* XRD, EPR, XANES, and FT-IR characterizations. J Catal, 2011, 278: 288–296
46 Shi J, Zhao M, Wang Y, *et al.* Upgrading of aromatic compounds in bio-oil over ultrathin graphene encapsulated Ru nanoparticles. J Mater Chem A, 2016, 4: 5842–5848
47 Chen S, Brown L, Levendorf M, *et al.* Oxidation resistance of graphene-coated Cu and Cu/Ni alloy. ACS Nano, 2011, 5: 1321–1327
48 Qu Y, Dai T, Cui Y, *et al.* Tailoring electronic structure of copper nanosheets by silver doping toward highly efficient electrochemical reduction of nitrogen to ammonia. Chem Eng J, 2022, 433: 133752
49 Wu J, Li JH, Yu YX. Theoretical exploration of electrochemical nitrate reduction reaction activities on transition-metal-doped h-BP. J Phys Chem Lett, 2021, 12: 3968–3975
50 Chen GF, Yuan Y, Jiang H, *et al.* Electrochemical reduction of nitrate to ammonia *via* direct eight-electron transfer using a copper-molecular solid catalyst. Nat Energy, 2020, 5: 605–613
51 Wang Y, Zhou W, Jia R, *et al.* Unveiling the activity origin of a copper-based electrocatalyst for selective nitrate reduction to ammonia. Angew Chem Int Ed, 2020, 59: 5350–5354
52 Hu T, Wang C, Wang M, *et al.* Theoretical insights into superior nitrate reduction to ammonia performance of copper catalysts. ACS Catal, 2021, 11: 14417–14427
53 Chen ZW, Lu Z, Chen LX, *et al.* Machine-learning-accelerated discovery of single-atom catalysts based on bidirectional activation mechanism. Chem Catal, 2021, 1: 183–195
54 Dang Y, Wu T, Tan H, *et al.* Partially reduced Ru/RuO_2 composites as efficient and pH-universal electrocatalysts for hydrogen evolution. Energy Environ Sci, 2021, 14: 5433–5443

Acknowledgements This work was supported by the Science and Technology Research Project of the Education Department of Jilin Province (47120) and the National Natural Science Foundation of China (51901083).

Author contributions Wang Z and Cui Y conceived and designed the experiments. Cui Y and Ding G performed the preparation of materials and electrochemical measurements. Ge X and Zhang W conducted the characterizations. Sun C and Jiang Q performed the DFT calculations. Wang Z, Zhu Y, Cui Y and Zhao M discussed the results and wrote the paper. All authors contributed to the general discussion.

Conflict of interest The authors declare that they have no conflict of interest.

Supplementary information Experimental details and supporting data are available in the online version of the paper.

Yuhuan Cui is a PhD candidate at the Department of Materials Science and Engineering, Jilin University. Her current research focuses on the catalyst design in electrochemical NH_3 synthesis from nitrogen and nitrates.

Changning Sun is a PhD candidate at the Department of Materials Science and Engineering, Jilin University. His current research focuses on the nitrogen reduction reaction based on the density functional theory.

Zhili Wang is a professor at the Department of Materials Science and Engineering, Jilin University. His research interests include the structure-property relationship of advanced materials and the development of nanomaterials and 3D nanoporous materials for energy and environment related applications.

纳米多孔Ru掺杂Cu协同调节反应中间体吸附与水分子解离促进电化学硝酸盐还原合成氨

崔玉环[1,2†], 孙昌宁[1†], 丁国鹏[1], 赵明[1], 葛欣[3], 张伟[3], 朱永福[1*], 王智力[1*], 蒋青[1*]

摘要 作为能源密集型Haber–Bosch工艺合成氨的一种新兴替代品, 电化学硝酸盐还原反应(NO_3RR)在可持续合成氨和废水处理方面受到了关注. 然而, 由于缺乏有效的电催化剂, NO_3RR目前仍然面临氨产率低和选择性差的问题. 本文报道了通过脱合金法制备的纳米双模式孔Ru掺杂Cu催化剂作为NO_3RR的电催化剂, 在−0.2 V *versus* RHE的电位下表现出29.63 ± 0.74 mg h^{-1} $mg_{cat.}^{-1}$的超高氨产率与97.3% ± 2.5%的法拉第效率, 优于大多数报道的催化剂. 密度泛函理论计算表明, 在Cu中掺杂Ru可以优化中间体的吸附能, 降低NO_3RR速控步骤的能垒. 此外, Ru原子可以促进H_2O的吸附/解离, 为含N中间体氢化为NH_3提供活性氢. 这项工作为NO_3RR等过程进行高性能催化剂的合理设计提供了新的途径.